Research Article

Journal of Environmental Nanotechnology

Multi-objective Optimization of Green MnO_2–Napier Fibre/Epoxy Nanocomposites Using an Integrated BBD–RSM–ANN–MOGWO–TOPSIS Framework

C. Kanmani Pappa[1], B. Rajesh Kumar[2*], A. Kadirvel[3], G. Gayathiri Devi[4], Sheik Sulaiman Sherfudeen[5] and Dhanasekaran Arumugam[6]

[1]Department of Electronics and Communication Engineering, Vel Tech Ranagarajan Dr Sagunthala R&D Institute of Science and Technology, Chennai, TN, India
[2]Department of Electrical and Electronics Engineering, M. Kumarasamy College of Engineering, Karur, TN, India
[3]Department of Mechanical Engineering, R.M.K. Engineering College, Kavaraipettai, Thiruvallur, TN, India
[4]Department of Science and Humanities, R.M.D. Engineering College, Kavaraipettai, Thiruvallur, TN, India
[5]Department of Mechanical Engineering, Francis Xavier Engineering College, Tirunelveli, TN, India
[6]Department of Mechanical Engineering, Academy of Maritime Education and Training (AMET), Deemed to be University, Kanathur, Chennai, TN, India
Received: 29.07.2026 Accepted: 31.08.2026 Published: xx.xx.xxxx
*rajuae2011@gmail.com

ABSTRACT

This study presents an integrated statistical and machine-learning framework for optimizing the mechanical performance of epoxy composites reinforced with alkali-treated Napier grass fibres and green-synthesized MnO_2 nanoparticles. A three-factor Box–Behnken design comprising 15 experimental runs was used to investigate molding pressure (2–6 MPa), molding temperature (80–120 °C), and MnO_2 loading (0.5–1.5 wt.%). The experimental responses ranged from 53.4 to 73.0 MPa for open-hole tensile strength (OHTS), 3.42 to 4.65 GPa for elastic modulus (EM), and 0.0161 to 0.0225 mm/mm for failure strain (FS). The developed quadratic models were highly significant ($p < 0.0001$), exhibited R^2 values above 0.997, and showed nonsignificant lack of fit. RSM desirability optimization identified a condition of 4.73 MPa, 104.5 °C, and 1.23 wt.% MnO_2, predicting an OHTS of 73.79 MPa, EM of 4.78 GPa, and FS of 0.0161 mm/mm. An MLP–ANN trained using the Levenberg–Marquardt algorithm achieved training R^2 values of 0.9957–0.9970 and leave-one-out cross-validation R^2 values of 0.9528–0.9595. The validated ANN was integrated with the multi-objective grey wolf optimizer to maximize OHTS and EM while minimizing FS, which was defined as a non-beneficial criterion representing the selected preference for a stiffer, lower-deformation composite. While RSM desirability provided a direct compromise based on the fitted quadratic models, ANN–MOGWO generated 100 non-dominated Pareto solutions, from which TOPSIS selected the final balanced solution using predefined response weights. The selected condition was 5.82 MPa, 103.8 °C, and 1.27 wt.% MnO_2, with predicted OHTS, EM, and FS values of 70.50 MPa, 4.62 GPa, and 0.0161 mm/mm, respectively. Unlike conventional RSM desirability optimization, the integrated approach enabled transparent evaluation and ranking of multiple trade-off solutions, with experimental confirmation errors of 0.97–1.24% for the selected condition. The proposed framework facilitates data-driven exploration of processing conditions and reduces the need for additional optimization experiments beyond the initial 15-run design. The optimized composites show potential for lightweight, moderately loaded structural components where enhanced stiffness, controlled deformation, and sustainable material selection.

Keywords: Green synthesis; Machine learning; Tensile strength; Elastic modulus; TOPSIS.

1. INTRODUCTION

The increasing demand for lightweight, sustainable, and high-performance natural fiber-reinforced polymer composites has accelerated research toward environmentally friendly materials for structural and engineering applications. Integrating machine learning with composite design has been demonstrated to efficiently optimize mechanical performance while reducing experimental cost and development time (Sonya *et al.* 2025). The incorporation of functional nanomaterials has become an effective approach for overcoming the limitations of conventional natural fiber composites (Ramalho *et al.* 2026). The incorporation of green-synthesized metal oxide nanoparticles has also emerged as an effective strategy for enhancing the mechanical, thermal, and durability characteristics of natural fiber composites (Jachak *et al.* 2026). MnO_2 was selected because its rigid inorganic structure, high surface activity, and rough particulate morphology can promote mechanical interlocking with epoxy, restrict polymer-chain mobility, and improve load transfer when adequately dispersed. Direct experimental evidence also supports MnO_2 as an epoxy nanofiller. (Balguri *et al.* 2022) reported that 0.1 wt.% MnO_2 nanoflowers increased tensile strength by 73%, elongation by 173%, and impact strength by 35%, while MnO_2 nanowires increased flexural strength by 15%. Hussain et al. further demonstrated that α-MnO_2 loading of 0.5, 0.75, and 1.0 wt.% and curing temperatures of 24–140 °C significantly affected epoxy-nanocomposite properties, supporting optimization of both filler loading and processing temperature. These effects are expected to increase stiffness and open-hole tensile performance while controlled nanoparticle loading can limit agglomeration-induced stress concentrations. Likewise, statistical optimization techniques combined with advanced nanofillers have facilitated the development of high-performance composites with minimized experimental effort (Raj *et al.* 2025).

Among the various lignocellulosic reinforcements, Napier grass (*Cenchrus purpureus*) has attracted considerable attention because of its rapid growth, abundant availability, low density, high cellulose content, and favorable mechanical properties. Kevlar/Napier grass hybrid epoxy laminates fabricated by the hand lay-up technique have demonstrated improved structural performance suitable for lightweight engineering applications (Ganesamoorthy *et al.* 2021). Napier grass fibers have also been successfully utilized as sustainable reinforcements in brake pad composites, providing enhanced thermal stability, friction behavior, and mechanical properties while reducing reliance on conventional synthetic materials (Kumar *et al.* 2022). Collectively, previous studies confirm the reinforcing potential of Napier grass; however, most investigate untreated or conventionally modified fibres without combining green metal-oxide nanofillers, controlled compression-molding parameters, and multi-response optimization. Consequently, the combined effects of fibre treatment, nanoparticle loading, and processing conditions on strength, stiffness, and failure deformation remain insufficiently resolved. Furthermore, chemically treated and naturally dyed Napier grass fibers have exhibited improved surface characteristics and fiber–matrix compatibility for environmentally friendly composite applications (Patil *et al.* 2024). The incorporation of Napier grass cellulose nanowhiskers into polylactic acid films has significantly improved tensile strength, crystallinity, and thermal stability, demonstrating their potential for biodegradable engineering materials (Sucinda *et al.* 2021). Although Napier fibre provides a sustainable reinforcement, its mechanical performance depends strongly on fibre–matrix adhesion, matrix consolidation, and processing quality. Incorporating MnO_2 nanoparticles offers a route to further modify stiffness and load transfer; however, nanoparticle benefits depend on loading and processing conditions because excessive addition can promote agglomeration. Therefore, molding pressure, temperature, and MnO_2 concentration must be optimized simultaneously rather than evaluated independently. The specific research gap addressed here is the limited understanding of alkali-treated Napier fibre/epoxy containing green-synthesized MnO_2 under simultaneous variation of molding pressure (2–6 MPa), molding temperature (80–120 °C), and MnO_2 loading (0.5–1.5 wt.%), considering OHTS, elastic modulus, and failure strain together.

Machine learning and statistical optimization techniques have increasingly been employed to improve the performance prediction of MnO_2-based materials in various engineering applications. Oxidative desulfurization performance of MnO_2-based catalysts has been accurately predicted using multilayer perceptron artificial neural networks (Humadi and Mohammed, 2026). The adsorption efficiency of MnO_2 materials for As(III) removal has been successfully optimized through Box–Behnken experimental design (Metta *et al.* 2025). Likewise, the thermal performance of MnO_2-enhanced photovoltaic–thermal collectors has been effectively predicted using Radial Basis Function neural networks, highlighting the capability of artificial intelligence for modeling complex material systems (Rajakumar *et al.* 2025).

Microstructural characterization plays an essential role in understanding the structure–property relationship of natural fiber composites. Scanning electron microscopy has been extensively employed to evaluate fiber morphology, interfacial adhesion, nanoparticle dispersion, and fracture mechanisms (Zhao *et al.* 2025). In addition, natural cellulose fibers have demonstrated excellent potential for sustainable papermaking and other renewable material applications (Dabadé *et al.* 2026). The optimization of Napier grass gasification parameters demonstrated that RSM can effectively predict process performance and identify optimum operating conditions for enhanced syngas production (Qatan *et al.* 2023). The extraction of bioactive compounds from Napier grass was successfully optimized using a Box–Behnken-based RSM approach, resulting in improved antioxidant and antimicrobial properties (Thaisungnoen *et al.* 2024). For composite-property optimization, BBD–RSM provides interpretable linear, interaction, and quadratic effects, ANN captures nonlinear input–response relationships, and multi-criteria methods enable balanced selection among competing mechanical responses (Boumaazaa *et al.* 2025). (Girmay *et al.* 2026) is retained only to demonstrate the applicability of BBD–RSM to MnO_2 processing. For composite systems involving competing mechanical responses, these predictive approaches can be further combined with evolutionary and decision-making methods to identify practical trade-off solutions rather than optimizing individual properties independently.

The adsorption performance of lignin-based nanocomposites derived from hybrid Napier grass was effectively enhanced through RSM optimization, confirming its capability for sustainable nanomaterial development (Behera *et al.* 2025). The application of organic mulches in Super Napier grass cultivation was statistically evaluated using an RSM-based experimental approach, demonstrating improved soil properties and weed control efficiency (Nohong *et al.* 2024). The functionalization of cellulose derived from Napier grass was optimized using RSM, leading to improved structural characteristics and superior adsorption performance for water treatment applications (Rangseesuriyachai *et al.* 2026). The co-digestion process of Napier grass with cattle dung was successfully optimized through Box–Behnken design and RSM, resulting in enhanced biogas production with excellent predictive accuracy (Warade *et al.* 2023). Furthermore, RSM was employed to optimize stirring conditions during the anaerobic digestion of Napier grass, significantly improving methane yield and reactor stability (Warade *et al.* 2025).

Despite separate investigations on Napier-fibre composites, MnO_2 nanomaterials, and statistical optimization, limited evidence exists on alkali-treated Napier fibre/epoxy composites reinforced specifically with green-synthesized MnO_2 nanoparticles. More importantly, the simultaneous influence of molding pressure, molding temperature, and MnO_2 loading on OHTS, elastic modulus, and failure strain has not been systematically integrated with predictive and Pareto-based optimization. The integrated framework was selected because each method addresses a distinct requirement. The methodological novelty lies not in the individual algorithms, but in their sequential integration: the 15-run BBD supplies experimental data, RSM quantifies statistical effects, ANN provides nonlinear surrogate predictions, MOGWO generates non-dominated trade-offs, and TOPSIS ranks these solutions to select one experimentally validated compromise. The novelty of this study lies in the combined development of alkali-treated Napier grass fibre/epoxy composites reinforced with orange-peel-mediated green-synthesized MnO_2 nanoparticles and their optimization through an integrated BBD–RSM–ANN–MOGWO–TOPSIS framework. The study simultaneously evaluates molding pressure (2–6 MPa), molding temperature (80–120 °C), and MnO_2 loading (0.5–1.5 wt.%**)** against three mechanical responses: OHTS, elastic modulus, and failure strain. Thus, novelty arises from the integration of the material system, green nanoparticle synthesis, simultaneous mechanical-response optimization, nonlinear prediction, Pareto search, and final compromise selection.

2. MATERIALS AND METHODOLOGY

2.1 Materials

Napier grass fibres were used as the primary reinforcement, while LY556 epoxy resin and HY951 hardener constituted the polymer matrix. The resin and hardener were mixed at a mass ratio of 10:1. Sodium hydroxide was used for fibre surface modification, and dilute acetic acid was employed for neutralization. Potassium permanganate ($KMnO_4$) served as the manganese precursor for the green synthesis of MnO_2 nanoparticles. Orange-peel extract was used as the phytochemical reducing and stabilizing medium. Distilled water and ethanol were used for solution preparation and nanoparticle purification.

2.2 Preparation and Treatment of Napier Grass Fibres

Napier grass stems were thoroughly washed with distilled water to remove soil and adhering contaminants and subsequently air-dried. Fibre bundles were separated from the stems through mechanical roller decortication, following the general extraction procedure (Thandavamoorthy and Devarajan, 2025). Approximately 285 g of dry fibres were obtained from 1.00 kg of dried Napier grass stems, corresponding to a fibre-extraction yield of 28.5%. The extracted fibres were cut to a uniform length of 50 ± 2 mm and had a mean diameter of 320 ± 45 µm.

The fibres were immersed in a 5 wt.% NaOH solution at a fibre-to-solution ratio of 1:20 g mL^{-1} for 4 h at 25 ± 2 °C. This treatment was intended to modify the fibre surface and potentially reduce portions of waxes, hemicellulose, lignin, and other loosely bound constituents. However, complete removal of these components is not claimed because their concentrations were not quantified before and after treatment.

Following alkali treatment, the fibres were neutralized using 1 vol.% acetic acid and repeatedly washed with distilled water until a final rinse pH of 7.0 ± 0.2 was obtained. The treated fibres were oven-dried at 60 °C for 24 h and conditioned at 23 ± 2 °C and 50 ± 5% relative humidity for 48 h. Finally, the dried fibres were stored in sealed moisture-resistant containers until composite fabrication.

2.3 Preparation of Orange-peel Extract

Fresh orange peels were washed thoroughly with distilled water, cut into small pieces and shade-dried. The dried peels were ground into powder and mixed with distilled water. The mixture was heated under continuous stirring to facilitate the extraction of polyphenols, flavonoids and other phytochemical constituents. After cooling, the suspension was filtered to obtain a clear extract. The prepared extract was used immediately as a reducing and stabilizing medium for MnO_2 nanoparticle synthesis.

2.4 Green Synthesis of MnO_2 Nanoparticles

A 100 mL volume of 0.01 M $KMnO_4$ was added dropwise to 20 mL of orange-peel extract, corresponding to a precursor-to-extract volume ratio of 5:1. The initial pH was adjusted to 6.5 ± 0.2. The reaction was maintained at 60 °C under continuous stirring at 500 rpm for 60 min and subsequently aged for 24 h. The resulting dark-brown precipitate was recovered by centrifugation at 10,000 rpm for 15 min. It was washed three times with distilled water and twice with ethanol. The purified precipitate was dried at 80 °C for 12 h and thermally treated at 400 °C for 2 h using a heating rate of 5 °C min^{-1}.During green synthesis, permanganate ions (MnO_4^-, Mn(VII)) from $KMnO_4$ undergo partial reduction to Mn(IV), producing MnO_2. Polyphenolic and flavonoid constituents of orange-peel extract can act as electron donors during this conversion. Under the near-neutral reaction condition (pH 6.5 ± 0.2), the reduction can be represented as:

$$MnO_4^- + 2H_2O + 3e^- \rightarrow MnO_2 + 4OH^-$$

Oxidized phytochemical species can subsequently adsorb onto the MnO_2 surface and contribute to particle stabilization and reduced uncontrolled growth. The reduction and stabilization pathway described above is a proposed mechanism based on permanganate chemistry and previous literature. It was not directly verified here by in-situ spectroscopy, phytochemical analysis, or oxidation-state measurements and should therefore not be interpreted as experimentally confirmed (Mladenova *et al.* 2024). The present SEM–EDS results confirm the presence of manganese and oxygen; however, they do not independently establish the Mn oxidation state, and definitive Mn(IV) confirmation would require techniques such as XPS.

2.5 Epoxy Matrix and MnO_2 Dispersion

MnO_2 loadings of 0.5, 1.0, and 1.5 wt.% were calculated relative to the mass of LY556 epoxy resin before HY951 hardener addition. MnO_2 was added incrementally to the LY556 epoxy resin and mechanically stirred at 600 rpm for 30 min. The suspension was then ultrasonicated at 20 kHz and 300 W for 20 min using a pulse cycle of 5 s on and 5 s off. A cooling bath maintained the mixture at 25 ± 2 °C. HY951 hardener was subsequently added at an epoxy-to-hardener mass ratio of 10:1 and gently mixed for 5 min. The mixture was vacuum-degassed at −0.09 MPa for 10 min before composite fabrication.

2.6 Composite Fabrication

The treated Napier grass fibres were maintained at a constant loading of 30 wt.%. Preliminary trials considered molding pressures of 1–7 MPa, temperatures of 70–130 °C, and MnO_2 loadings of 0–2.0 wt.%. Pressures below 2 MPa produced inadequate consolidation, whereas pressures above 6 MPa caused excessive resin loss. Temperatures below 80 °C produced insufficient curing, while temperatures above 120 °C caused laminate discoloration. MnO_2 loadings above 1.5 wt.% produced visible agglomeration and increased mixture viscosity. Therefore, 2–6 MPa, 80–120 °C, and 0.5–1.5 wt.% were selected. The fibres were arranged in the mold and impregnated with the MnO_2-containing epoxy mixture. Composite laminates were fabricated using compression molding under the pressure and temperature combinations specified by the Box–Behnken design (Tunali *et al.* 2026). The molding duration was maintained at 15 min, and laminates with a nominal thickness of 3 mm were produced. After demolding, the composites were post-cured at 80 °C for 2 h and conditioned before specimen preparation and mechanical testing.

2.7 Morphological and Eelemental Characterization of Green-synthesized MnO_2 Nanoparticles

The surface morphology and elemental composition of the green-synthesized MnO_2 nanoparticles were examined using scanning electron microscopy (SEM) coupled with energy-dispersive X-ray spectroscopy (EDS). The SEM micrographs obtained at different magnifications are presented in Fig. 1a and b, while the corresponding EDS spectrum is shown in Fig. 1c.

The SEM micrographs of the green synthesized MnO_2 nanoparticles at different magnifications are shown in Fig. 1(a–b). The larger individual particle of MnO_2 shows an irregular fractal shape as shown in Figure 1(a). The particle has a layered structure of rough edges, micro-voids, and uneven surfaces, with small grains of MnO_2 attached to the bigger flakes. The multi-layered structure enhances the surface roughness and creates many anchor sites for polymer adhesion. Therefore, the observed morphology is a desirable aspect for enhancing the overall mechanical properties of the epoxy composites reinforced with MnO_2.

The synthesized manganese-oxide material exhibited agglomerated flake-like and plate-like structures with finer granular surface features as shown in figure 1(b). The agglomeration is believed to be due to the high surface energy of the nanoparticles and the adsorption of phytochemical components from the plant extract applied in the green synthesis procedure. The rough surface texture and irregular stacking of the flakes suggest the presence of interconnected MnO_2 aggregates.

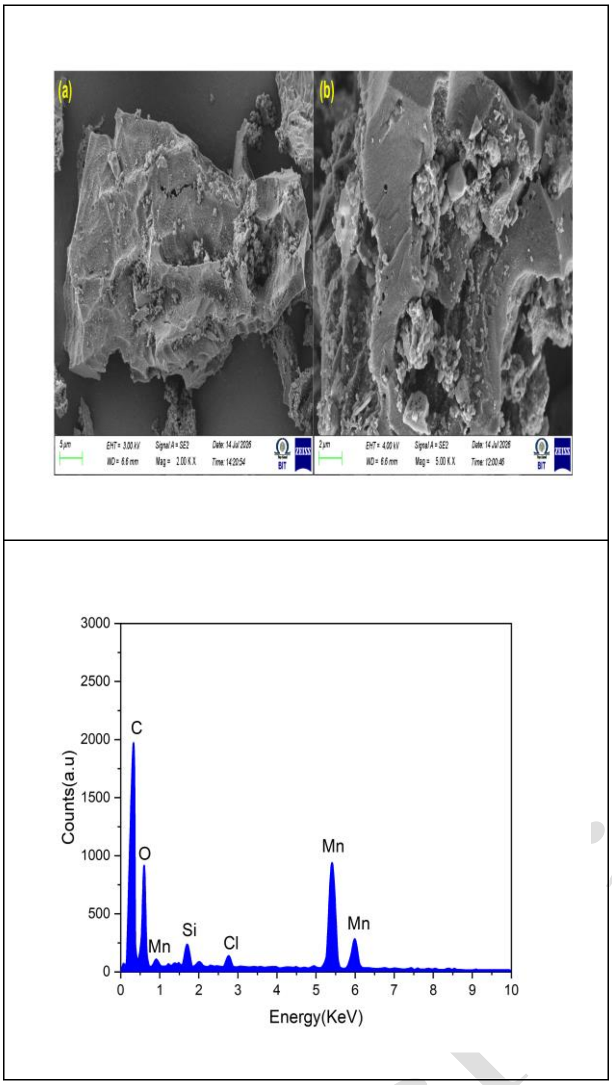

Fig. 1: Morphological and elemental characterization of green-synthesized MnO_2 nanoparticles: (a) SEM micrograph at 2.00 K X, (b) SEM micrograph at 5.00 K X and (c) EDS spectrum

The EDS spectrum in Fig. 1c displayed prominent Mn and O signals, supporting the formation of a manganese-oxide product. However, SEM–EDS cannot distinguish MnO_2 from other manganese oxides or determine the Mn oxidation state; consequently, MnO_2 phase identity is not claimed from SEM–EDS alone. Minor carbon signals may be attributed to residual plant-derived organic compounds, the conductive coating or the carbon adhesive used during sample preparation. The absence of intense peaks associated with unwanted elements indicated the relative purity of the synthesized material. The combined SEM–EDS observations confirmed the presence of MnO_2 nanoparticles and their suitability for incorporation into the Napier grass fibre/epoxy composite. XRD, XPS, TEM, and DLS measurements were not performed; therefore, the crystalline phase, Mn oxidation state, and primary particle-size distribution are not quantitatively claimed. SEM observations at 2.00 KX and 5.00 KX are restricted to describing the agglomerated flake-/plate-like morphology.” The manuscript currently reports those two SEM magnifications but no defensible nanoparticle-size value.

2.8 Fabrication of Napier Grass Fibre/MnO_2/Epoxy Composites

Napier grass fibre-reinforced epoxy composites containing green-synthesized MnO_2 nanoparticles were fabricated through compression molding (Sureshkumar *et al.* 2026). The procedure was designed to ensure adequate fibre impregnation, homogeneous nanoparticle dispersion and effective interfacial bonding. Molding pressure, molding temperature and MnO_2 loading were varied according to the Box–Behnken experimental design. The selected factor ranges were 2–6 MPa, 80-120 °C, and 0.5–1.5 wt.%, respectively, as illustrated in Fig. 2. Napier grass fibre content was maintained at 30 wt.% for all experimental runs.

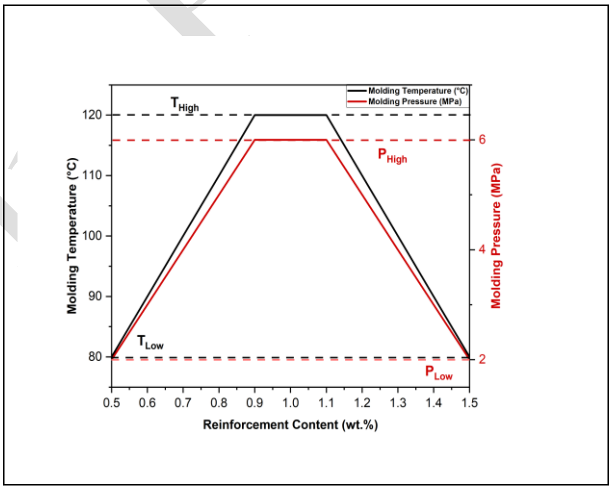

Fig. 2: Levels of the compression-molding parameters

The complete fabrication workflow is summarized in Fig. 3. A 300 × 300 mm steel mold was cleaned and release-coated, after which treated fibres were arranged uniformly, impregnated with the pre-dispersed MnO_2/epoxy mixture, and rolled to remove entrapped air. Laminates were compression-molded according to the BBD conditions for 15 min, cooled under pressure, post-cured at 80 °C for 2 h, and trimmed to approximately 300 × 300 × 3 mm. Detailed fibre treatment and nanoparticle-dispersion procedures are provided in Sections 2.2 and 2.5. Napier grass stems were initially washed to remove soil and adhering contaminants, after which the fibre bundles were mechanically separated. The extracted fibres were immersed in a 5 wt.% NaOH solution to remove surface waxes, hemicellulose, lignin and other loosely bonded constituents. Following alkali treatment, fibres was washed repeatedly by distilled water, neutralized using dilute acetic acid and rinsed until approximately neutral pH was obtained. The treated fibres were subsequently oven-dried to remove absorbed moisture and stored under dry conditions before composite fabrication. The dried fibres were cut to uniform dimensions compatible with the mold.

Fig. 3: Fabrication sequence of green-synthesized MnO_2-modified Napier grass fibre/epoxy composites

The required quantity of green-synthesized MnO_2 nanoparticles was calculated relative to the mass of the epoxy resin. Before dispersion, the nanoparticles were dried to remove physically adsorbed moisture. MnO_2 was then added incrementally to the LY556 epoxy resin and mixed using a mechanical stirrer. Ultrasonication was subsequently applied to break weak agglomerates and improve nanoparticle distribution. During ultrasonication, the mixture was maintained in a cooling bath to limit temperature elevation and prevent premature changes in resin viscosity.

Following nanoparticle dispersion, HY951 hardener was added to the MnO_2-containing epoxy resin at an epoxy-to-hardener mass ratio of 10:1. The mixture was stirred gently to achieve uniform curing-agent distribution while minimizing air entrapment. The resulting resin mixture was degassed before being applied to the fibre reinforcement.

A steel mold measuring 300 × 300 mm was cleaned thoroughly and coated with a suitable release agent. The treated Napier grass fibres were arranged uniformly within the mold, and the MnO_2-modified epoxy mixture was applied progressively to ensure complete fibre impregnation. A roller was used to distribute the resin and remove entrapped air. After completion of the lay-up, molds were closed and transferred to a compression-molding press.

Molding temperature and pressure were adjusted according to the corresponding BBD experimental run. Pressure was applied gradually to obtain uniform laminate consolidation and to prevent fibre displacement or excessive resin loss. Each laminate was maintained under the selected molding condition for 15 min. The mold was subsequently allowed to cool while maintaining pressure to minimize residual stresses and dimensional distortion.

After demolding, the laminates were post-cured at 80 °C for 2 h to promote completion of the epoxy crosslinking reaction. The fabricated plates had nominal dimensions of 300 × 300 × 3 mm. Excess material was trimmed from the laminate edges, and the plates were conditioned before machining the mechanical-test specimens.

2.9 Open-hole Tensile Test

Open-hole tensile testing was conducted to determine the tensile performance of the Napier grass fibre/MnO_2/epoxy composites in the presence of a geometrical stress concentration. The test were performed with ASTM D5766/D5766M. Rectangular specimens measuring 200 mm in length, 30 mm in width and 3 mm in thickness were machined from the fabricated composite laminates. A central hole with a diameter of 5.0 ± 0.05 mm was drilled in each specimen. Based on the specimen width of 30 mm, the width-to-hole-diameter ratio (W/D) was 6.0.

Drilling parameters were controlled to minimize edge damage, fibre pull-out and delamination around the hole. The hole surfaces were visually inspected before testing, and specimens containing pronounced machining defects were excluded.

The specimens were tested using a universal testing machine with an appropriate load capacity. Open-hole tensile loading was applied at a constant crosshead displacement rate of 2 mm min^{-1} under laboratory conditions of 30 ± 2 °C and 55 ± 5% relative humidity. Serrated grips were used to prevent specimen slippage, and careful alignment was maintained to minimize unintended bending during loading. A minimum of three specimens were tested for each experimental condition, and the results were expressed as mean values with the corresponding standard deviations.

The open-hole tensile strength was calculated using:

$$\sigma_{\mathrm{OHTS}} = \frac{P_{\max}}{wt} \qquad \dots (1)$$

where σ_{OHTS} is the open-hole tensile strength, P_{max} is the maximum applied load, w is the specimen width and t is the specimen thickness. Elastic modulus was determined from the linear region of the stress-strain curve, while failure strain was obtained from the strain recorded at specimen fracture.

2.10 Selection of Process Parameters

Molding pressure, molding temperature and MnO_2 nanoparticle loading were selected as the independent variables because they considerably influence composite consolidation, resin curing, nanoparticle dispersion, void formation and fibre–matrix interfacial bonding. Each factor was investigated at three levels.

Table 1. Factors and levels used in the Box–Behnken design

Factor	Symbol	Unit	Low (−1)	Centre (0)	High (+1)
Molding pressure	A	MPa	2	4	6
Molding temperature	B	°C	80	100	120
MnO_2 nanoparticle loading	C	wt.%	0.5	1.0	1.5

The fixed fabrication conditions were 30 wt.% Napier grass fibre, 5% NaOH treatment, a 10:1 epoxy–hardener ratio, a molding duration of 15 min, a laminate thickness of 3 mm and post-curing at 80 °C for 2 h.

2.11 Box–Behnken Experimental Design

A three-factor, three-level Box–Behnken design was employed to evaluate the linear, interaction and quadratic effects of the selected processing parameters. The design consisted of 12 edge-midpoint experiments and three replicated centre-point experiments, resulting in 15 runs. Centre-point replication was used to estimate pure experimental error and verify process repeatability. The experimental conditions were randomized using a computer-generated sequence to minimize systematic effects associated with fabrication order. The runs were conducted in the randomized order 13, 5, 2, 10, 7, 1, 14, 4, 11, 6, 9, 15, 3, 12, and 8. The three-factor BBD consisted of 12 factorial edge points and three centre-point runs, resulting in 15 experimental conditions. Each run represented a separately prepared resin mixture and independently fabricated laminate. The three centre-point runs were independently prepared to estimate pure experimental error and assess process repeatability. The complete actual-factor matrix and measured responses are presented in Table 3.

2.12 Response Measurement and Model Development

Open-hole tensile strength (OHTS), elastic modulus (EM) and failure strain (FS) were selected as the output responses. OHTS and elastic modulus were treated as beneficial responses and maximized, whereas failure strain was minimized to obtain a stiff composite with limited deformation.

A second-order polynomial model was fitted separately for each response:

$$Y = \beta_0 + \sum_{i=1}^{3} \beta_i X_i + \sum_{i=1}^{3} \beta_{ii} X_i^2 + \sum_{i<j}^{3} \beta_{ij} X_i X_j + \varepsilon \quad \ldots (2)$$

where Y represents OHTS, EM or FS; X_i and X_j represent the coded process variables; β_0 is the intercept; β_i, β_{ii} and β_{ij} are the linear, quadratic and interaction coefficients, respectively; and ε is the experimental error.

2.13 Statistical Analysis and Optimization

Analysis of variance was employed to assess model significance and the effects of individual model terms at a 95% confidence level. Model adequacy was evaluated using the model p-value, lack-of-fit, coefficient of determination, adjusted and predicted R^2, adequate precision, coefficient of variation and residual diagnostics. Numerical desirability optimization was performed by maximizing OHTS and elastic modulus while minimizing failure strain within the investigated factor ranges. The predicted optimal condition was subsequently verified through triplicate confirmation experiments.

2.14 Dataset Preparation for Machine Learning

The experimental dataset generated through the 15-run Box-Behnken design was used to develop the machine-learning model. Molding pressure, molding temperature, and MnO_2 nanoparticle loading were considered the input variables, while elastic modulus, failure strain and open-hole tensile strength, were treated as output responses. The input and output matrices were expressed as:

$$X = [P, T, C] \qquad Y = [OHTS, EM, FS] \quad \ldots (3)$$

where P, T and C represent molding pressure, molding temperature, and MnO_2 loading, respectively. Before ANN development, all input and output variables were consistently normalized to the range of −1 to +1 to ensure comparable numerical scales and stable network convergence. During each LOO-CV iteration, the withheld observation was excluded from ANN training and weight adjustment and was used only for independent prediction. Normalization was performed using:

$$X_n = 2\left(\frac{X - X_{\min}}{X_{\max} - X_{\min}}\right) - 1 \qquad \dots (4)$$

where X_n is the normalized value and $X_{\min}$ and $X_{\max}$ are the minimum and maximum values of the corresponding variable.

2.15 Development of the MLP-ANN Model

A feed-forward multilayer perceptron ANN was developed to establish nonlinear relationships between the processing parameters and mechanical responses. The ANN employed a 3–12–8–3 architecture comprising three input neurons corresponding to molding pressure, molding temperature, and MnO_2 loading; two hidden layers containing 12 and 8 neurons; and three output neurons representing OHTS, elastic modulus, and failure strain. Hyperbolic-tangent sigmoid activation functions were used in the hidden layers, whereas a linear activation function was used in the output layer. The network was trained using the Levenberg–Marquardt backpropagation algorithm for a maximum of 1000 epochs. Mean squared error was used as the performance function, and 20 independent initializations were conducted to reduce sensitivity to the initial weights and biases (Dongale *et al.* 2015).

Table 2. Configuration of the developed MLP-ANN model

ANN Parameter	Selected Setting
Input variables	Molding pressure, molding temperature and MnO_2 loading
Output variables	OHTS, elastic modulus and failure strain
Network architecture	3-12-8-3
Hidden-layer activation	Hyperbolic-tangent sigmoid (tansig)
Output-layer activation	Linear (purelin)
Training algorithm	Levenberg-Marquardt (trainlm)
Performance function	Mean squared error
Input/output normalization	-1 to +1
Maximum epochs	1000
Maximum validation failures	6
Independent initializations	20
Model validation	Leave-one-out cross-validation

2.16 ANN Performance Evaluation

The predictive performance of the MLP-ANN was evaluated using the coefficient of determination (R^2), root mean square error (RMSE), mean absolute error (MAE) and mean absolute percentage error (MAPE):

$$R^2 = 1 - \frac{\sum_{i=1}^{n} (Y_i - \hat{Y}_i)^2}{\sum_{i=1}^{n} (Y_i - \bar{Y})^2} \qquad \dots (5)$$

$$RMSE = \sqrt{\frac{1}{n}\sum_{i=1}^{n} \left(Y_i - \hat{Y}_i\right)^2} \qquad \dots (6)$$

$$MAE = \frac{1}{n}\sum_{i=1}^{n} \left|Y_i - \hat{Y}_i\right| \qquad \dots (7)$$

$$MAPE = \frac{100}{n}\sum_{i=1}^{n} \left|\frac{Y_i - \hat{Y}_i}{Y_i}\right| \qquad \dots (8)$$

where $Y_i, \hat{Y}_i$ and $\bar{Y}$ denote the experimental, ANN-predicted and mean experimental values, respectively. Leave-one-out cross-validation was employed to assess model generalization. During each iteration, one observation was withheld as test data, while the remaining 14 observations were used for ANN training. The withheld observation was subsequently predicted. This procedure was repeated 15 times so that every observation served once as independent test data. The combined withheld predictions were used to calculate the LOO-CV R^2, RMSE, MAE, and MAPE.

2.17 ANN-assisted Multi-objective Optimization

The validated ANN was integrated with the multi-objective grey wolf optimizer and employed as a surrogate response evaluator. This approach enabled rapid evaluation of candidate processing conditions without requiring additional physical experiments during optimization.

The decision vector was defined as:

$$\mathrm{x} = [P, T, C] \qquad \dots (9)$$

The optimization objectives were formulated as:

$$f_1(\mathrm{x}) = -OHTS_{\mathrm{ANN}}(\mathrm{x}) \qquad \dots (10)$$

$$f_2(\mathrm{x}) = -EM_{\mathrm{ANN}}(\mathrm{x}) \qquad \dots (11)$$

$$f_3(\mathrm{x}) = FS_{\mathrm{ANN}}(\mathrm{x}) \qquad \dots (12)$$

2.18 TOPSIS-based Compromise Selection

Because the Multi-Objective Grey Wolf Optimizer (MOGWO) generated multiple non-dominated solutions, the technique for order preference by similarity to an ideal solution was employed to identify a single balanced processing condition. OHTS and elastic modulus were treated as beneficial criteria, whereas failure strain was considered a non-beneficial criterion.

2.19 Experimental Confirmation

The processing condition selected through the ANN-MOGWO-TOPSIS framework was validated through an independent confirmation experiment. At least three composite specimens were fabricated at the selected molding pressure, molding temperature and MnO_2 loading. The measured responses were reported as mean ± standard deviation and compared with the ANN-MOGWO predictions.

The absolute prediction error was calculated as:

$$\text{Error}(\%) = \left|\frac{Y_{\text{exp}} - Y_{\text{pred}}}{Y_{\text{pred}}}\right| \times 100 \quad \ldots (13)$$

where Y_{exp} and Y_{pred} represent the experimental mean and ANN-MOGWO-predicted response, respectively. Model agreement was evaluated using relative error, RMSE, MAE, MAPE, and 95% confidence intervals without imposing arbitrary percentage thresholds. During each LOO-CV iteration, one observation was withheld as independent test data, while the remaining 14 observations were used for training. This procedure was repeated 15 times so that every observation served once as the withheld sample. The combined predictions were evaluated using R^2, RMSE, MAE, and MAPE. RSM provided quadratic desirability optimization, whereas ANN–MOGWO generated Pareto solutions that were subsequently ranked using TOPSIS.

3. RESULTS AND DISCUSSION

The mechanical performance of the Napier grass fibre/green-synthesized MnO_2/epoxy composites was investigated through an integrated experimental and computational framework. The Box–Behnken design (BBD) was initially employed to generate the experimental combinations, followed by response surface methodology (RSM) and analysis of variance (ANOVA) to quantify the linear, interaction and quadratic effects of the processing parameters. Subsequently, a multilayer perceptron artificial neural network (MLP–ANN) was developed to predict open-hole tensile strength (OHTS), elastic modulus (EM) and failure strain (FS). The validated ANN was integrated with the multi-objective grey wolf optimizer (MOGWO), and TOPSIS was used to identify the most balanced solution from the resulting Pareto archive.

3.1 Box–Behnken Experimental Responses

The BBD considered molding pressure, molding temperature and MnO_2 nanoparticle loading as the independent processing variables. The corresponding low, centre and high levels were 2, 4 and 6 MPa for pressure; 80, 100 and 120 °C for temperature; 0.5, 1.0 and 1.5 wt.% for MnO_2 loading, respectively. The Napier grass fibre content, NaOH concentration, epoxy-to-hardener ratio, molding duration, laminate thickness and post-curing conditions were maintained constant throughout the experiments. This approach allowed the effects of the three selected processing variables to be evaluated independently of changes in material composition and curing history.

The complete BBD matrix and the experimentally measured mechanical responses are reported in Table 3.

Table 3. BBD factors and actual factor levels

Run	P (MPa)	T (°C)	MnO_2 (wt.%)	OHTS (MPa)	EM (GPa)	FS (mm/mm)
1	2	80	1.0	53.4	3.47	0.0225
2	6	80	1.0	64.9	4.22	0.0177
3	2	120	1.0	63.1	4.03	0.0193
4	6	120	1.0	69.7	4.55	0.0162
5	2	100	0.5	54.8	3.42	0.0221
6	6	100	0.5	62.3	3.96	0.0181
7	2	100	1.5	58.0	3.88	0.0200
8	6	100	1.5	68.7	4.61	0.0161
9	4	80	0.5	55.9	3.50	0.0212
10	4	120	0.5	63.8	3.98	0.0185
11	4	80	1.5	61.9	4.14	0.0192
12	4	120	1.5	67.5	4.46	0.0165
13	4	100	1.0	72.1	4.60	0.0171
14	4	100	1.0	73.0	4.65	0.0174
15	4	100	1.0	72.4	4.58	0.0170

Runs 13, 14, and 15 all correspond to 4 MPa, 100 °C, and 1.0 wt.% MnO_2. Their respective OHTS values were 72.1, 73.0, and 72.4 MPa; elastic moduli were 4.60, 4.65, and 4.58 GPa; and failure strains were 0.0171, 0.0174, and 0.0170 mm/mm. The OHTS ranged from 53.4 to 73.0 MPa, while the elastic modulus varied between 3.42 and 4.65 GPa. Failure strain ranged from 0.0161 to 0.0225 mm/mm. A summary of the minimum, maximum and mean response values is provided in Table 4.

Table 4. Experimental response ranges and best observed runs

Response	Minimum	Maximum	Overall Mean
Open-hole tensile strength (OHTS)	53.4 MPa	73.0 MPa	64.10 MPa
Elastic modulus (EM)	3.42 GPa	4.65 GPa	4.137 GPa
Failure strain (FS)	0.0161 mm/mm	0.0225 mm/mm	0.01859 mm/mm

Runs 13–15 collectively represented the centre condition and produced mean OHTS, elastic modulus, and failure-strain values of 72.50 MPa, 4.610 GPa, and

0.01717 mm/mm, respectively. In contrast, the minimum failure strain of 0.0161 mm/mm was observed for Run 8 at 6 MPa, 100 °C and 1.5 wt.% MnO_2. These results indicate that improved laminate consolidation and nanoparticle-assisted stiffening generally enhanced strength and modulus while reducing deformation at failure. However, the highest values were not consistently obtained at the upper limits of all variables, suggesting the presence of nonlinear and interaction effects. These nonlinear response trends support the use of BBD–RSM to quantify interaction and quadratic effects of molding pressure, temperature, and MnO_2 loading on composite mechanical performance. Box–Behnken design optimized the operating conditions, enabling complete phenol removal within 30 min while demonstrating excellent catalyst stability and reusability (Liu *et al.* 2021).

3.2 Centre-point Repeatability

Runs 13–15 were independently fabricated replicates of the BBD centre condition of 4 MPa molding pressure, 100 °C molding temperature, and 1.0 wt.% MnO_2 loading. These replicates were used to estimate pure experimental error and assess process repeatability. The calculated centre-point means, standard deviations and coefficients of variation are presented in Table 5.

Table 5. Repeatability of the replicated BBD centre point

Response	Mean	Standard Deviation	CV (%)
Open-hole tensile strength (OHTS)	72.50 MPa	0.458 MPa	0.632
Elastic modulus (EM)	4.610 GPa	0.036 GPa	0.782
Failure strain (FS)	0.01717 mm/mm	0.000208 mm/mm	1.213

For n = 3 centre-point replicates, OHTS was 72.50 ± 0.458 MPa (CV = 0.632%), elastic modulus was 4.610 ± 0.036 GPa (CV = 0.782%), and failure strain was 0.01717 ± 0.000208 mm/mm (CV = 1.213%). All CV values were below 2%, indicating satisfactory centre-point repeatability." These values agree with Runs 13–15. The OHTS values of 72.1, 73.0, and 72.4 MPa for Runs 13–15 produced a centre-point mean of 72.50 ± 0.458 MPa. The coefficients of variation were 0.632% for OHTS, 0.782% for elastic modulus and 1.213% for failure strain. All values were below 2%, demonstrating satisfactory repeatability in composite fabrication and mechanical testing. The limited variation among the centre-point replicates also provided a reliable estimate of pure error for evaluating the lack of fit of the quadratic response model.

3.3 RSM Model Adequacy and Process-variable Effects

Second-order polynomial models were developed using the coded variables A, B and C, representing molding pressure, molding temperature and MnO_2 loading, respectively. The resulting coded equations for OHTS, elastic modulus, and failure strain are given in Eqs. (14)–(16).

$$OHTS = 72.500 + 4.5375A + 3.5000B + 2.4125C - 5.5250A^2 - 4.2000B^2 - 6.0250C^2 - 1.2250AB + 0.8000AC - 0.5750BC \quad \ldots (14)$$

$$EM = 4.610 + 0.3175A + 0.21125B + 0.27875C - 0.2975A^2 - 0.2450B^2 - 0.3450C^2 - 0.0575AB + 0.0475AC - 0.0400BC \quad \ldots (15)$$

$$FS = 0.017167 - 0.001975A - 0.0012625B - 0.0010125C + 0.0009917A^2 + 0.0007667B^2 + 0.0009167C^2 + 0.000425AB + 0.000025AC \quad \ldots (16)$$

The positive linear coefficients in Eqs. (14) and (15) indicate that pressure, temperature and MnO_2 loading initially enhanced OHTS and elastic modulus. Conversely, the negative quadratic coefficients demonstrate that excessive increases in these variables eventually reduced the mechanical responses, resulting in internal maxima within the investigated design space. For failure strain, the negative linear and positive quadratic coefficients indicate an initial decrease followed by the development of a shallow minimum.

The ANOVA and model-adequacy statistics are summarized in Table 6.

Table 6. ANOVA and goodness-of-fit statistics for the developed quadratic response models

Statistical Parameter	OHTS	Elastic Modulus	Failure Strain
Model F-value	599.57	409.79	225.77
Model p-value	<0.0001	<0.0001	<0.0001
Coefficient of determination, (R^2)	0.9991	0.9986	0.9975
Adjusted (R^2)	0.9974	0.9962	0.9931
Predicted (R^2)	0.9950	0.9917	0.9803
Adequate precision	70.3	54.2	45.9
Lack-of-fit p-value	0.8876	0.8496	0.7288

The quadratic models were highly significant for OHTS, elastic modulus and failure strain, with model F-values of 599.57, 409.79 and 225.77, respectively, and $p < 0.0001$ in all cases. The respective R^2 values were 0.9991,0.9986 and 0.9975, indicating that more than 99.7% of the experimental variation was explained by the fitted models.

The adjusted and predicted R^2 values were in close agreement for all three responses. Adequate precision values of 70.3,54.2 and 45.9 were substantially greater than the recommended minimum value of 4, confirming an adequate signal-to-noise ratio. Furthermore, the lack-of-fit p-values were 0.8876 for OHTS, 0.8496 for elastic modulus and 0.7288 for failure strain. The nonsignificant lack of fit demonstrates that the unexplained model variation was comparable with pure experimental error rather than being associated with systematic model inadequacy.

For OHTS and elastic modulus, the linear terms A, B and C, all two-factor interactions and all quadratic terms were statistically significant at the 95% confidence level. For failure strain, the three linear terms, the AB interaction and the quadratic terms were significant, whereas the AC and BC interactions were nonsignificant.

The response contour for the combined effects of molding pressure and temperature on OHTS at 1.0 wt.% MnO_2 is presented in Fig. 4.

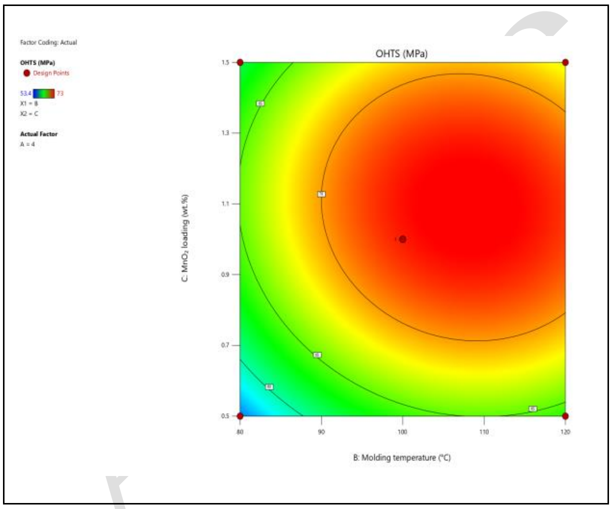

Fig. 4: OHTS response contour for molding pressure and temperature at 1.0 wt.% MnO_2

Increasing pressure and temperature from their lower levels produced a substantial increase in OHTS. Greater molding pressure improved laminate consolidation, reduced entrapped air and increased effective contact between the treated Napier grass fibres and the epoxy matrix. Increasing temperature reduced resin viscosity and promoted fibre wetting and cure development. The contour curvature suggests that strength reduction at excessive processing conditions may be associated with resin squeeze-out, premature curing, or thermally induced residual stresses. Figure 5 presents the pressure–temperature interaction for elastic modulus at 1.0 wt.% MnO_2.

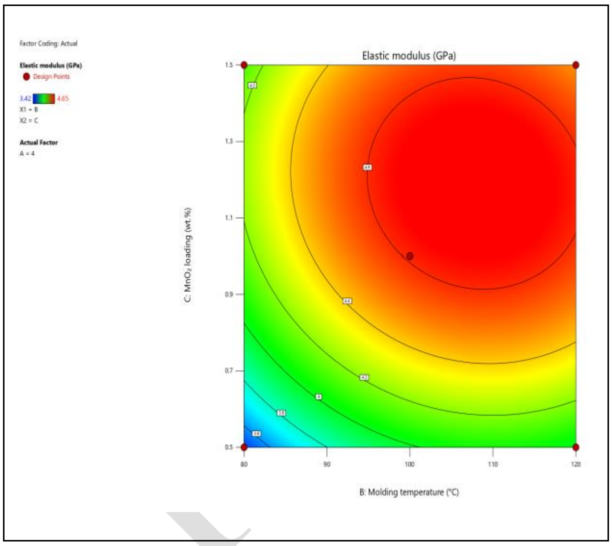

Fig. 5: Elastic-modulus response contour for molding pressure and temperature at 1.0 wt.% MnO_2

The modulus increased toward the central-to-upper region of the design space, indicating the formation of a more rigid composite structure. Improved compaction enhanced fibre–matrix load transfer, while controlled heating promoted matrix crosslinking. The negative quadratic coefficients suggest that stiffness reduction may be associated with local fibre damage, matrix embrittlement, or resin-depleted regions; however, these mechanisms were not directly quantified. The corresponding failure-strain contour is shown in Fig. 6.

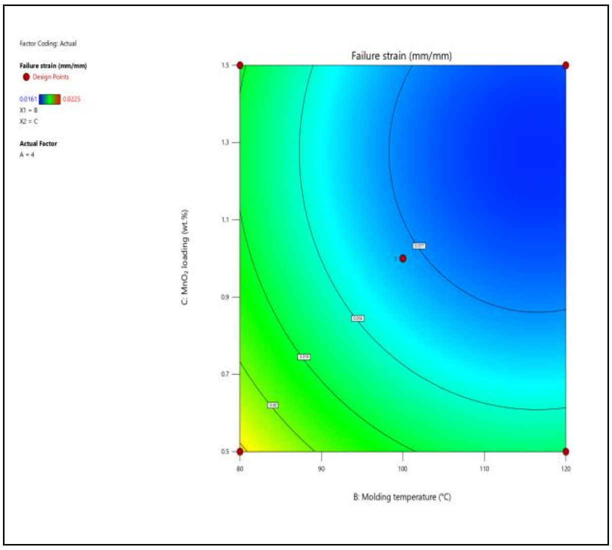

Fig. 6: Failure-strain response contour for molding pressure and temperature at 1.0 wt.% MnO_2

Failure strain decreased with increasing pressure and temperature, indicating reduced deformation as the composite became more rigid. However, excessively low failure strain also indicates reduced ductility; therefore, it was considered together with strength and modulus during multiresponse optimization. The lowest predicted strain occurred in the high-pressure and moderate-to-high-temperature region. This inverse relationship between modulus and failure strain is consistent with the development of a stiffer fibre–matrix network. However, excessively low failure strain may also indicate reduced ductility; therefore, it was considered together with strength and modulus during multiresponse optimization. Interpretations involving reduced void content, resin-viscosity changes, enhanced crosslinking, polymer-chain restriction, and improved interfacial stress transfer are proposed explanations consistent with the response trends and SEM morphology. These mechanisms were not directly quantified through void-fraction measurements, DSC/DMA, interfacial shear testing, or spectroscopic interfacial characterization and are therefore not presented as experimentally verified.

3.4 RSM Desirability Optimization and Confirmation

A desirability-function approach was employed to determine a processing condition that simultaneously maximized OHTS and elastic modulus and minimized failure strain. OHTS was maximized over 53.4–73.0 MPa, elastic modulus over 3.42–4.65 GPa, and failure strain was minimized over 0.0161–0.0225 mm/mm. Linear desirability functions with unit weights and equal importance were used, and overall desirability was calculated as their geometric mean. The optimum processing variables and predicted responses are summarized in Table 7.

Table 7. Optimal processing conditions and predicted mechanical responses obtained through RSM desirability optimization

Parameter or Response	RSM-optimized Value
Molding pressure	4.730 MPa
Molding temperature	104.543 °C
MnO_2 nanoparticle loading	1.2327 wt.%
Predicted open-hole tensile strength	73.7898 MPa
Predicted elastic modulus	4.7757 GPa
Predicted failure strain	0.0160975 mm/mm
Overall desirability	1.000

The RSM optimization identified a molding temperature of 104.543 °C, a molding pressure of 4.730 MPa, and an MnO_2 loading of 1.2327 wt.% as the preferred processing condition. At this point, the model predicted an OHTS of 73.7898 MPa, an elastic modulus of 4.7757 GPa and a failure strain of 0.0160975 mm/mm. The overall desirability value was 1.000, indicating that the specified response goals were simultaneously satisfied within the selected factor ranges. The confirmation results obtained at the RSM optimum are compared with the model predictions in Table 8.

Table 8. Experimental validation of the RSM-predicted optimal responses

Mechanical Response	RSM-predicted Value	Experimental Value (mean ± SD)	Absolute Error (%)
Open-hole tensile strength (MPa)	73.7898	73.800 ± 0.200	0.014
Elastic modulus (GPa)	4.7757	4.760 ± 0.020	0.328
Failure strain (mm/mm)	0.0160975	0.0161167 ± 0.0000351	0.119

Three independently fabricated specimens were tested at the RSM optimum. The experimental OHTS, elastic modulus, and failure strain were 73.800 ± 0.200 MPa, 4.760 ± 0.020 GPa, and 0.0161167 ± 0.0000351 mm/mm, respectively. Their 95% confidence intervals were 73.303–74.297 MPa, 4.710–4.810 GPa, and 0.016030–0.016204 mm/mm, respectively. The experimental means remained within the corresponding 95% prediction intervals, supporting agreement between the RSM predictions and confirmation results.The corresponding absolute prediction errors were 0.014%, 0.328% and 0.119%. All confirmation means were within the 95% prediction intervals, demonstrating good agreement between the RSM predictions and the experimental observations.

3.5 Predictive Performance of the MLP–ANN

An MLP–ANN was developed using molding pressure, molding temperature and MnO_2 loading as the input variables and OHTS, elastic modulus and failure strain as the outputs. The input and output variables were normalized between −1 and 1. The network was trained using the Levenberg–Marquardt algorithm with a hyperbolic-tangent sigmoid activation function in the hidden layer and a linear activation function in the output layer. The ANN fitting and leave-one-out cross-validation results are presented in Table 9.

Table 9. Predictive performance of the MLP–ANN model under training and leave-one-out cross-validation

Response	ANN Training R^2	ANN LOO-CV R^2	ANN RMSE	ANN MAE	ANN MAPE (%)	RSM LOO-CV R^2	RSM RMSE	RSM MAE	RSM MAPE (%)
OHTS	0.9966	0.9529	1.3623	1.1032	1.7691	0.9950	0.4461	0.3800	0.5886

Elastic modulus	0.9970	0.9595	0.08505	0.07414	1.8210	0.9917	0.03851	0.03333	0.8054
Failure strain	0.9957	0.9528	0.0004375	0.0003451	1.8292	0.9803	0.0002823	0.0002467	1.3410

The LOO-CV R^2 values remained between 0.9528 and 0.9595, while MAPE values ranged from 1.7691% to 1.8292%. Cross-validated residuals were distributed around zero without systematic trends. These results demonstrate that the high training performance was reasonably retained for withheld observations and provide no clear evidence of substantial overfitting within the investigated BBD domain. The training R^2 values were 0.9966, 0.9970, and 0.9957, while the corresponding LOO-CV R^2 values were 0.9529, 0.9595, and 0.9528 for OHTS, elastic modulus, and failure strain, respectively. The LOO-CV R^2 values above 0.95 indicated satisfactory internal validation within the investigated BBD dataset; however, they do not constitute independent external validation.

The RMSE values were 1.3623 MPa for OHTS, 0.08505 GPa for elastic modulus and 0.0004375 mm/mm for failure strain. The corresponding MAPE values ranged from 1.77% to 1.83%, demonstrating relatively low prediction errors compared with the measured response ranges. The agreement between the experimental and ANN-predicted responses is illustrated in Fig. 7.

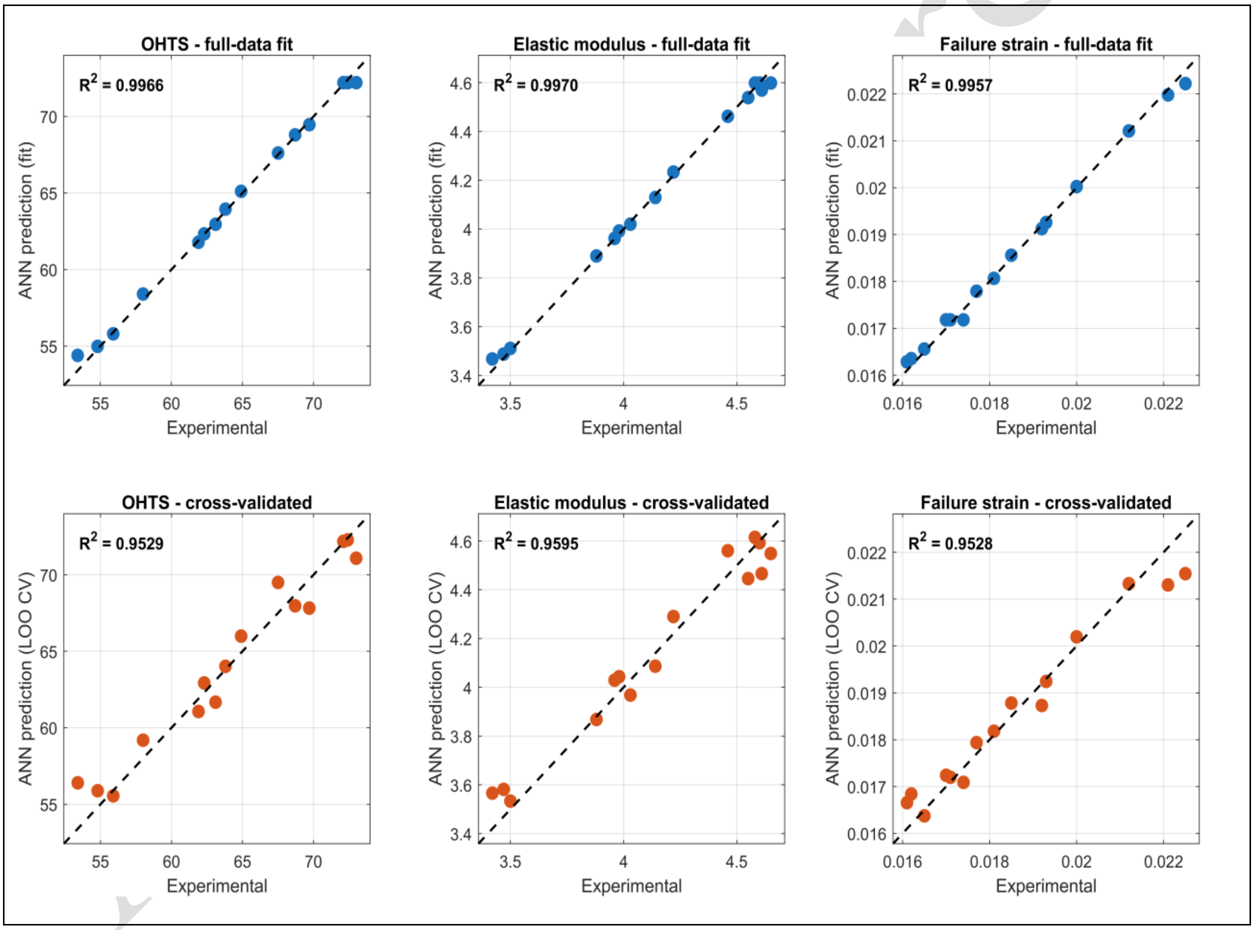

Fig. 7: Experimental versus ANN-predicted responses for the full-data fit and leave-one-out cross-validation

The predicted values were closely distributed around the line of equality for all three responses, confirming that the ANN captured the principal nonlinear relationships between the processing variables and mechanical properties. Nevertheless, the greater dispersion in the LOO-CV predictions compared with the training results reflects the limited number of unique experimental observations. The cross-validated residual distributions are presented in Fig. 8.

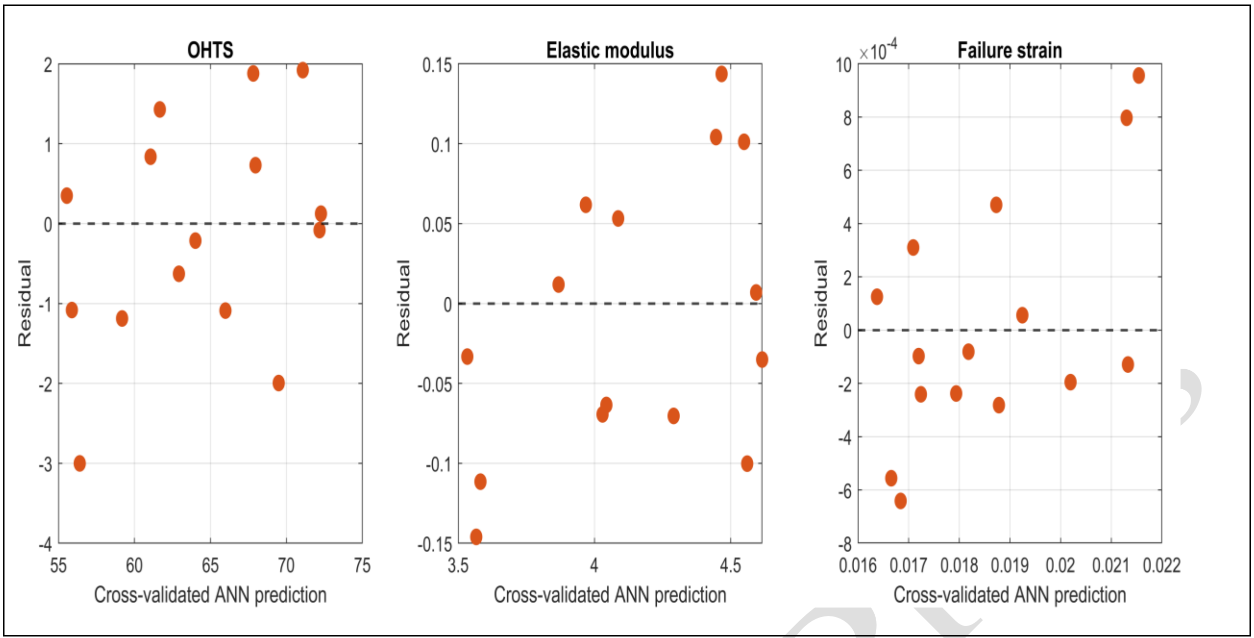

Fig. 8: Residual distributions for the cross-validated ANN predictions

The residuals were distributed around zero without a systematic increasing or decreasing pattern, indicating the absence of substantial model bias. The corresponding error histograms in Fig. 9 show that most prediction errors were concentrated near zero, further supporting the predictive suitability of the developed ANN within the selected experimental region.

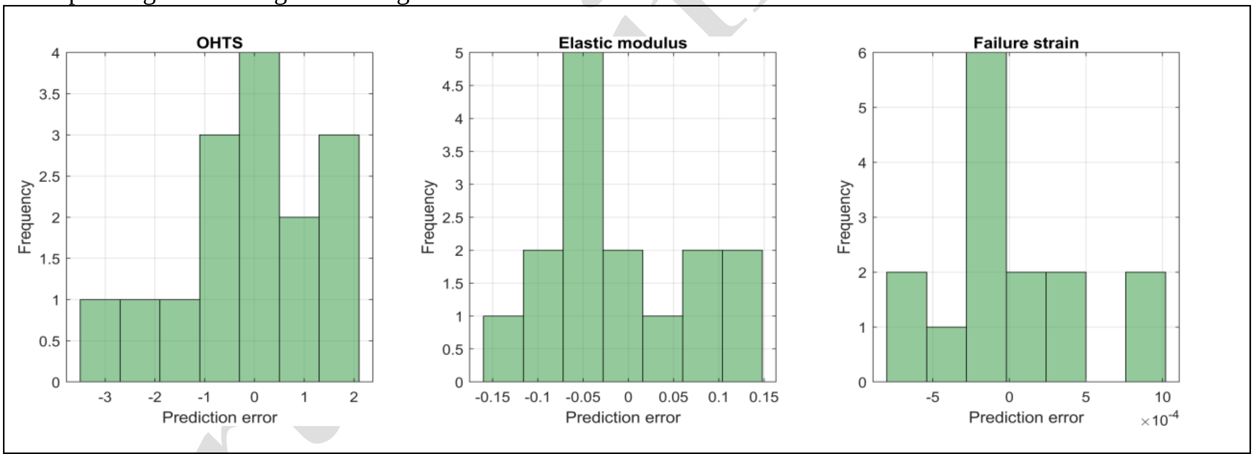

Fig. 9: Error histograms for OHTS, elastic modulus and failure strain

3.6 ANN-assisted MOGWO Optimization

The validated ANN was subsequently integrated with MOGWO and used as a computationally efficient surrogate for evaluating candidate processing conditions. The multi-objective problem was formulated to maximize OHTS and elastic modulus while minimizing failure strain. All candidate solutions were constrained to the experimentally investigated BBD ranges: 2–6 MPa for molding pressure, 80–120 °C for molding temperature, and 0.5–1.5 wt.% for MnO_2 loading. Candidate positions exceeding these limits were returned to the nearest permissible boundary before ANN evaluation. Consequently, MOGWO did not use ANN extrapolation outside the training domain.

The algorithm employed 50 search agents, 200 iterations, an archive capacity of 100 solutions and 10 grid divisions. Twenty independent runs were conducted to evaluate the consistency of the optimization process. Convergence histories were averaged across the 20 independent runs, and their standard deviations were used to quantify run-to-run variability. Mean ± SD bands were added to Fig. 10. The processing variables were constrained to the original BBD ranges of 2–6 MPa, 80–120 °C and 0.5–1.5 wt.% MnO_2, thereby preventing unsupported extrapolation beyond the experimental domain. The mean archive growth and Pareto-spacing histories are presented in Fig. 10.

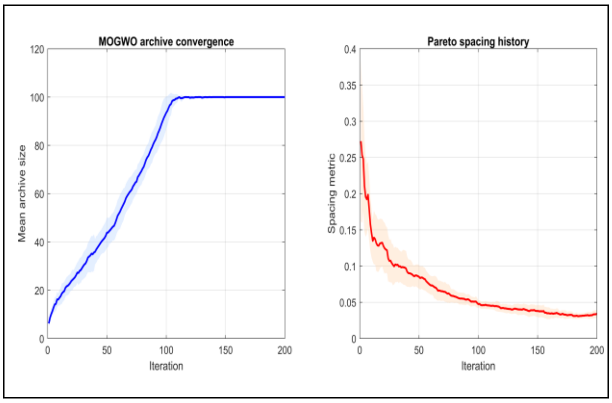

Fig. 10: Mean archive growth and pareto-spacing history

The archive size reached its specified capacity of 100 solutions; this indicated archive saturation only and was not interpreted as evidence of convergence. Convergence assessment was based on 20 independent MOGWO runs using 50 search agents, 200 iterations, a 100-solution archive, and 10 grid divisions. Mean ± SD histories quantified run-to-run variability. Pareto spacing decreased from approximately 0.27 initially to approximately 0.03 at iteration 200. Reaching the 100-solution archive capacity was interpreted only as archive saturation, not convergence. The spacing value decreased from approximately 0.27 during the initial iterations to nearly 0.03 at the end of the optimization, indicating an increasingly uniform distribution of the Pareto solutions. The final three-dimensional Pareto front is presented in Fig. 11.

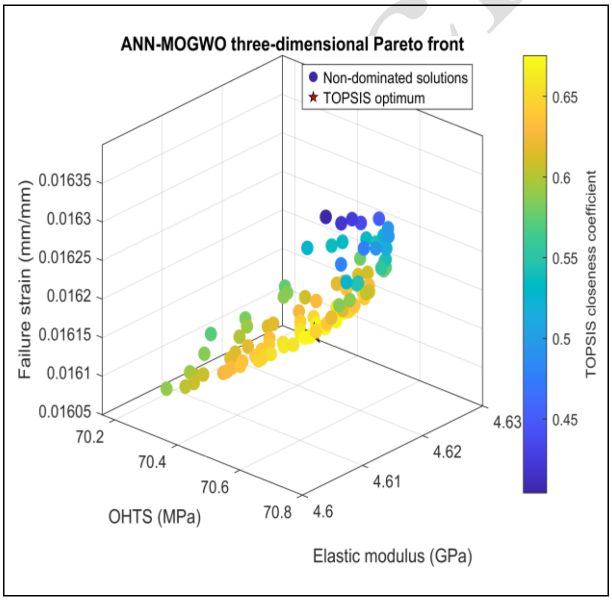

Fig. 11: ANN–MOGWO three-dimensional Pareto front coloured by TOPSIS closeness coefficient

Each point represents a non-dominated trade-off among OHTS, elastic modulus and failure strain. The Pareto front demonstrates that simultaneous improvement of all responses was not possible without compromise. Solutions with high elastic modulus and low failure strain did not necessarily provide the maximum OHTS, confirming the need for a multi-criteria selection method.

The distributions of molding pressure, molding temperature, and MnO_2 loading were examined for all non-dominated solutions. The concentration of solutions within the moderate-to-high pressure region indicates the importance of adequate laminate consolidation. Temperature and MnO_2 loading were distributed around intermediate values, consistent with the quadratic response behaviour identified through RSM.

3.7 TOPSIS Compromise Selection

TOPSIS was applied to the final MOGWO archive to select a single compromise solution. The criterion directions and weights are presented in Table 10. Failure strain was minimized to favour dimensional stability; however, lower strain does not necessarily indicate improved toughness or ductility. Failure strain was treated as non-beneficial only for the selected design objective of a stiff, dimensionally stable component and not as a universal measure of superior composite performance. Because excessive minimization could favour brittle behaviour, failure strain received the lowest weight (0.25), compared with 0.40 for OHTS and 0.35 for elastic modulus. Lower failure strain is therefore interpreted as controlled deformation, not improved toughness or ductility.

Table 10. TOPSIS criteria, preference directions and weighting coefficients used for Pareto-solution ranking

Performance Criterion	Criterion Type	Weighting Coefficient
Open-hole tensile strength (OHTS)	Beneficial	0.40
Elastic modulus (EM)	Beneficial	0.35
Failure strain (FS)	Non-beneficial	0.25

The TOPSIS weights were assigned according to the intended performance priorities of moderately loaded, dimensionally stable composite components. OHTS received the highest weight of 0.40 because resistance to open-hole failure was the principal requirement. Elastic modulus received a weight of 0.35 because structural stiffness was the secondary requirement. Failure strain received a lower weight of 0.25 because controlled deformation was considered important but subordinate to strength and stiffness. The weights summed to unity and were applied consistently to all Pareto solutions. The resulting TOPSIS closeness coefficients and rankings were calculated for all archived Pareto solutions. The highest closeness coefficient identifies the solution positioned closest to the positive ideal condition and farthest from the negative ideal condition. The final compromise condition selected by the integrated ANN–MOGWO–TOPSIS framework is summarized in Table 11.

Table 11. Optimal compromise solution selected using the integrated ANN–MOGWO–TOPSIS framework

Processing Parameter or Predicted Response	Selected Value
Pareto solution number	19
Molding pressure	5.8240 MPa
Molding temperature	103.764 °C
MnO_2 nanoparticle loading	1.2735 wt.%
Predicted open-hole tensile strength	70.5032 MPa
Predicted elastic modulus	4.6174 GPa
Predicted failure strain	0.0161442 mm/mm
TOPSIS closeness coefficient	0.6753
TOPSIS rank	1

Pareto Solution 19 achieved the highest closeness coefficient of 0.6753 and was therefore assigned Rank 1. The selected processing condition consisted of molding temperature of 103.764 °C a molding pressure of 5.8240 MPa and MnO_2 loading of 1.2735 wt.%.

At this condition, the ANN predicted an OHTS of 70.5032 MPa, an elastic modulus of 4.6174 GPa and a failure strain of 0.0161442 mm/mm. The selected OHTS was slightly lower than the maximum experimental value because TOPSIS did not optimize strength independently. Instead, the method selected a balanced compromise that retained high strength and stiffness while maintaining a low failure strain.

Compared with Run 4, Solution 19 increased OHTS by 0.803 MPa and modulus by 0.067 GPa while reducing failure strain by 0.000056 mm/mm. Compared with Run 8, it increased OHTS by 1.803 MPa and modulus by 0.007 GPa, with failure strain increasing by only 0.000044 mm/mm. Its factors remained within the BBD ranges, confirming interpolation rather than extrapolation. These runs combined high pressure with elevated temperature or MnO_2 loading and produced comparatively high strength and modulus together with low failure strain. This agreement confirms that the TOPSIS-selected solution remained physically consistent with the experimental response trends.

The RSM and ANN–MOGWO–TOPSIS optimization routes produced different preferred processing conditions because they employ different decision mechanisms. RSM desirability identifies a local compromise directly from the fitted quadratic equations, whereas MOGWO generates a population of non-dominated solutions before TOPSIS applies the selected response weights. Therefore, the difference between the two optima represents the distinct optimization strategies rather than a contradiction between the models. This comparison demonstrates that RSM desirability and ANN–MOGWO–TOPSIS serve different optimization purposes: direct response compromise and Pareto-based multi-objective decision-making, respectively. Hybrid MCDM approaches combined with fuzzy TOPSIS successfully identified the optimum nanofluid by considering thermal conductivity, viscosity, and heat capacity (Kumar *et al.* 2025). The practical advantage of ANN–MOGWO–TOPSIS is not lower prediction error: RSM confirmation errors were only 0.014–0.328%. Instead, the integrated framework generated 100 non-dominated alternatives and ranked them explicitly using OHTS, EM, and FS weights of 0.40, 0.35, and 0.25. Solution 19 achieved the highest TOPSIS coefficient of 0.6753 and gave confirmation errors of 0.969%, 1.243%, and 1.089% for OHTS, EM, and FS, respectively.

3.8 Final Confirmation of the ANN–MOGWO–TOPSIS Solution

The ANN–MOGWO–TOPSIS condition was experimentally validated at 5.824 MPa, 103.764 °C, and 1.2735 wt.% MnO_2. Three independently fabricated specimens were tested, and the results were reported as mean ± SD and compared with ANN predictions using absolute relative error. The ANN–MOGWO predictions and experimentally measured confirmation results are presented in Table 12.

Table 12. Confirmation of the ANN–MOGWO–TOPSIS predictions

Mechanical Response	ANN–MOGWO Prediction	Confirmation (Mean ± SD)	Absolute Error (%)
Open-hole tensile strength (MPa)	70.5032	69.82 ± 0.35	0.969
Elastic modulus (GPa)	4.6174	4.560 ± 0.040	1.243
Failure strain (mm/mm)	0.0161442	0.016320 ± 0.000120	1.089

Confirmation errors were 0.014–0.328% for RSM and 0.969–1.243% for ANN–MOGWO–TOPSIS, which additionally enabled Pareto-based compromise selection. Based on three independent specimens, the 95% confidence intervals were 68.95–70.69 MPa, 4.461–4.659 GPa, and 0.016022–0.016618 mm/mm for OHTS, elastic modulus, and failure strain, respectively.

The SEM micrographs presented in Fig. 12 illustrate the fractured surfaces of the confirmation specimens and reveal the damage mechanisms governing the tensile failure of the Napier grass fibre/MnO_2/epoxy composite.

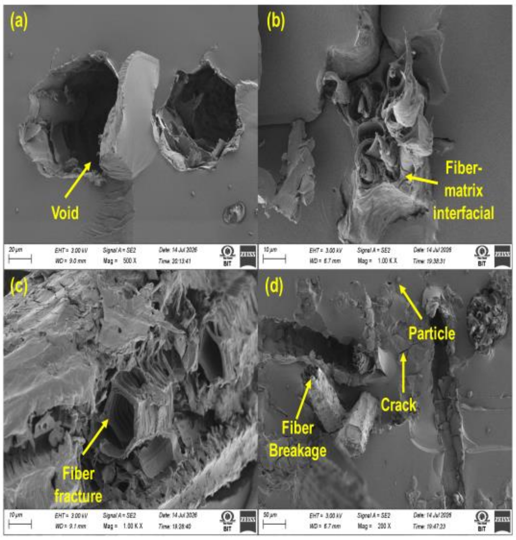

Fig. 12: SEM micrographs of the fractured open-hole tensile specimen produced under the ANN–MOGWO–TOPSIS-selected processing condition: (a) Void, (b) Fiber matrix Interfacial, (c) Fiber Fracture and (d) Fiber Breakage and MnO_2 nanoparticle agglomeration

The SEM micrographs presented in Fig. 12 illustrate the fracture morphology of the open-hole tensile specimen fabricated under the optimized processing condition. The examined fracture region was located along the cross-section of the central hole, where stress concentration promoted damage initiation and subsequent crack propagation.

In Figure 12(a), large voids in the fractured composite are clearly visible. They can occur as a result of entrapped air, failure to infiltrate resin into the cavities, or localized fibre pull-out during compression molding and subsequent mechanical failure. Such voids can cause discontinuities in the composite structure and may serve as local stress-concentration locations. When loaded in tension, cracks may nucleate around these areas and then grow in the surrounding epoxy matrix. Hence, it is important to reduce the void content in the composite by proper resin impregnation and consolidation to enhance mechanical integrity. In previous studies, SEM analysis revealed significant disruption and roughening of the Napier grass fibre surface after biological hydrolysis, indicating effective degradation of the lignocellulosic structure. The observed morphological changes confirmed enhanced fibre accessibility for biomass conversion (Shen *et al.* 2026).

Figure 12(b) displays the fibre-matrix interface, where the fibres have broken apart, causing some to be exposed to the epoxy matrix. The presence of matrix material associated with the surface of the fibre can be related to some degree of interfacial interaction and mechanical interlocking between the fibres of Napier grass and epoxy. Regional gaps and separation, however, suggest that debonding at the interface played a role in the fracture process. The fracture morphology is rough and irregular and this indicates that the fracture was not the result of simple brittle failure of matrix but a result of a mixture of matrix deformation, inter-facial separation and fibre damage.

In Fig. 12(c), a distinct fracture of the fibre is seen along with the characteristic hollow lumen and layered structure of the natural fibre. The fracture surface was not smooth, but it was splintered and broke into a fibrillated area where the Napier grass fibre was split and ruptured during loading. The rupture of the fibres is indicative of transfer of at least some of the applied stress from the epoxy matrix to the fibres before final failure. The fractured matrix and debonding at the interfaces also suggest a combination of matrix cracking, fibre splitting, fibre fracturing and debonding.

Figure 12(d) shows a broken fibre–matrix region and a localized spherical feature of undetermined composition within the matrix. The surrounding matrix shows cracking and localized deformation and fibre breakage shows mechanical loading on the reinforcement. If the compositional analysis confirms the presence of Mn and O at this feature, then the spherical shape could be interpreted as an MnO_2 particle or agglomerate. Localized particulate features may act as stress-concentration sites; however, their composition was not established.

At the ANN–MOGWO–TOPSIS-selected condition, measured OHTS, elastic modulus, and failure strain were 69.82 ± 0.35 MPa, 4.560 ± 0.040 GPa, and 0.016320 ± 0.000120 mm/mm, respectively, compared with ANN predictions of 70.5032 MPa, 4.6174 GPa, and 0.0161442 mm/mm. Fibre rupture and retained matrix on fibre surfaces are consistent with effective load transfer and the relatively high stiffness, whereas voids, interfacial gaps, fibre pull-out, and matrix cracking indicate localized damage that may restrict strength development. These SEM correlations are morphological evidence and are not interpreted as direct causal proof.

These findings demonstrate that the optimized processing condition provided a favourable balance between composite consolidation, fibre–matrix bonding and nanoparticle reinforcement. Further improvements may be achieved by enhancing MnO_2 dispersion, reducing air entrapment, controlling resin viscosity and improving interlaminar impregnation. Such modifications could suppress premature crack initiation and delamination, thereby improving the strength, stiffness and structural reliability of Napier grass fibre/MnO_2/epoxy composites.

4. CONCLUSIONS

This study developed an integrated BBD–RSM–ANN–MOGWO–TOPSIS framework to model and optimize the mechanical performance of Napier grass fibre/green-synthesized MnO_2/epoxy composites. The 15-run BBD demonstrated that molding pressure, molding temperature, and MnO_2 loading significantly influenced OHTS, elastic modulus, and failure strain, while the replicated centre points showed coefficients of variation below 2%. The statistically significant quadratic models, nonsignificant lack of fit, and close confirmation results supported the adequacy of RSM within the investigated experimental domain.

- RSM desirability optimization identified a condition of 4.730 MPa, 104.543 °C, and 1.2327 wt.% MnO_2, predicting an OHTS of 73.7898 MPa, an elastic modulus of 4.7757 GPa, and a failure strain of 0.0160975 mm/mm. In contrast, ANN–MOGWO generated multiple non-dominated trade-offs, from which TOPSIS selected 5.8240 MPa, 103.764 °C, and 1.2735 wt.% MnO_2 as the final balanced compromise. The corresponding predicted OHTS, elastic modulus, and failure strain were 70.5032 MPa, 4.6174 GPa, and 0.0161442 mm/mm, respectively. RSM provided a single direct desirability optimum at 4.730 MPa, 104.543 °C, and 1.2327 wt.% MnO_2, with confirmation errors of 0.014–0.328%. In contrast, ANN–MOGWO–TOPSIS generated 100 non-dominated alternatives and transparently ranked competing OHTS–EM–FS trade-offs, selecting 5.8240 MPa, 103.764 °C, and 1.2735 wt.% MnO_2. Therefore, its principal advantage over RSM is explicit Pareto-based decision flexibility and transparent compromise selection rather than superior prediction accuracy.

- The ANN achieved LOO-CV R^2 values of 0.9528–0.9595 and MAPE values below 1.83%, indicating good internal predictive performance within the studied factor ranges. However, these results do not establish external generalizability because the ANN was developed using only 15 experimental observations. The coded regression coefficients indicated that molding pressure exerted the greatest influence on the three mechanical responses. Moderate MnO_2 loading was associated with improved composite stiffness; however, enhanced interfacial stress transfer was not claimed without direct interfacial characterization.

- Fracture-surface SEM revealed voids, fibre pull-out, interfacial gaps, matrix cracking, and fibre rupture, which were consistent with mixed-mode failure rather than conclusively confirming the complete fracture mechanism. Feature-specific elemental analysis was unavailable; therefore, localized particulate features were not definitively assigned to MnO_2 agglomeration.

- The optimized composite shows potential for lightweight, moderately loaded structural components requiring high stiffness and controlled deformation; however, application-specific durability, toughness, environmental, and long-term performance tests remain necessary. Future studies should improve particle dispersion, reduce void content, investigate different fibre loadings, expand the experimental dataset, and independently validate the computational optimization framework**.**

FUNDING

This research received no specific grant from any funding agency in the public, commercial, or not-for-profit sectors.

CONFLICTS OF INTEREST

The authors declare that there is no conflict of interest.

COPYRIGHT

REFERENCES

Balguri, P. K., Thumu, U., Harris Samuel, D. G., Penki, T. R. and Chilumala, I., Manganese dioxide nanostructures reinforced epoxy nanocomposites: a study of mechanical properties, *Polym. Plast. Technol. Mater.*, 61(4), 441–460 (2022). https://doi.org/10.1080/25740881.2021.1991953

Behera, S., Rath, S., Mohapatra, S., Chandra, B. B. and Thatoi, H., Hybrid synthesis of Carboxymethylated-Lignin-Tetra ethoxysilane nanocomposite for adsorption of hexavalent chromium, *Separat. Purif. Technol.*, 359 130861 (2025). https://doi.org/10.1016/j.seppur.2024.130861

Boumaazaa, M., Belaadi, A., Hassan, A., Ibrahim, A. M. H. and Djamel, G., Modeling and Optimization of Tensile Properties of Epoxy Biocomposites Reinforced with *Washingtonia robusta* Waste and Biochar Using Response Surface Methodology, Artificial Neural Networks, and Multi-Criteria

Decision-Making, *J. Nat. Fib.*, 22(1), 2540475 (2025). https://doi.org/10.1080/15440478.2025.2540475

Dabadé, D. S., Koumassa, O. A. B., Adékambi, A. O., Hounsou, M., Götz, B., Kreyenschmidt, J. and Hounhouigan, D. J., Evaluation of Cyperus articulatus, Cenchrus purpureus and Imperata cylindrica characteristics as sustainable raw materials for pulp and paper production in Benin, West Africa, *Biores. Technol. Rep.*, 34, 102704 (2026). https://doi.org/10.1016/j.biteb.2026.102704

Dongale, T. D., Jadhav, P. R., Navathe, G. J., Kim, J. H., Karanjkar, M. M. and Patil, P. S., Development of nano fiber MnO_2 thin film electrode and cyclic voltammetry behavior modeling using artificial neural network for supercapacitor application, *Mater. Sci. Semicond. Proc.*, 36, 43–48 (2015). https://doi.org/10.1016/j.mssp.2015.02.084

Ganesamoorthy, R., Meenakshi Reddy, R., Raja, T., Panda, P. K., Dhoria, S. H., Nasif, O., Alfarraj, S., Manikandan, V. and Jenish, I., Studies on Mechanical Properties of Kevlar/Napier Grass Fibers Reinforced with Polymer Matrix Hybrid Composite, *Adv. Mater. Sci. Eng.*, 2021(1), 6907631 (2021). https://doi.org/10.1155/2021/6907631

Girmay, H. A., Choi, Y., Hong, J., Kang, H., Sabir, F. K., Amenu, G., Kwon, J., Lee, J., Tufa, L. T. and Gonfa, B. A., Strategic Mass Optimization of MnO_2 Nanostructures Synthesized via Coprecipitation: A Response Surface Methodology (RSM)-Guided Electrochemical Study, *Inorg. Chem.*, 65(25), 13863–13877 (2026). https://doi.org/10.1021/acs.inorgchem.6c00900

Humadi, J. I. and Mohammed, W. T., Hybrid experimental: ANN approach for rapid dibenzothiophene oxidation in oscillatory reactor using coated magnetic carbonaceous catalyst, *J. Iran. Chem. Soc.*, 23(8), 243 (2026). https://doi.org/10.1007/s13738-026-03535-6

Jachak, S. R., Srinivasan, R., Arunkumar, S., Kumar, V. N., Manu, Y. M. and Mayakannan, S., Development of MUF-bonded Banyan Fiber Laminates Reinforced with Bio-synthesized CeO_2 Nanoparticles for Advanced Applications, *J. Environ. Nanotechnol.*, 15(2), 554–562 (2026). https://doi.org/10.13074/jent.2026.06.2622149

Kumar, D., Dikshit, M. K., Chaudhary, N., Pathak, V. K. and Singh, R., Selection of nano powder mixed dielectric fluid (NPMDF) in electric discharge machining using hybrid multi-criteria decision-making method, *Discover Appl. Sci.*, 7(4), 275 (2025). https://doi.org/10.1007/s42452-025-06719-6

Kumar, N., Singh, A., Singh, S., Singh, J. I. P. and Kumar, S., Napier natural fibre used as reinforcement polymer composite: As asbestos free brake friction material, *Mater. Today: Proc.*, 56, 2532–2536 (2022). https://doi.org/10.1016/j.matpr.2021.09.006

Liu, X., Zhou, J., Liu, D., Li, L., Liu, W., Liu, S. and Feng, C., Construction of Z-scheme $CuFe_2O_4/MnO_2$ photocatalyst and activating peroxymonosulfate for phenol degradation: Synergistic effect, degradation pathways, and mechanism, *Environ. Res.*, 200, 111736 (2021). https://doi.org/10.1016/j.envres.2021.111736

Metta, S. R., Sahu, U. K., Sahu, M. K., Mohanty, H. S., Kar, P., Application of Box-Behnken Design Model for Statistical Optimization of As(III) Removal Using Iron Manganese Bimetal Oxide Composite, *ChemistrySelect*, 10(17), e202406130 (2025). https://doi.org/10.1002/slct.202406130

Mladenova, B., Pashova, K., Hinkov, I., Dimitrova, M. and Stoyanova, A., Green synthesis of MnO_2 using Calendula officinalis and Tilia cordata extracts for application in supercapacitors, *Monatshefte für Chemie*, 155(3–4), 341–348 (2024). https://doi.org/10.1007/s00706-024-03179-3

Nohong, B., Sudarsono and Rinduwati, Effect of Organic Mulches on Weed Dynamics and Productivity of Super Napier Grass, *Agri. Sci. Digest*, 44(5), 843–848 (2024). https://doi.org/10.18805/ag.DF-620

Patil, H., Yadav, S. and Athalye, A., Valorisation of Napier grass through fibre extraction and coloration by natural dye from Rubia tinctorum, *Coloration Technol.*, 140(6), 858–867 (2024). https://doi.org/10.1111/cote.12747

Qatan, H. S. O., Wan Ab Karim Ghani, W. A. and Md Said, M. S., Prediction and optimization of syngas production from Napier grass air gasification via kinetic modelling and response surface methodology, *Energy*, 270, 126883 (2023). https://doi.org/10.1016/j.energy.2023.126883

Raj, M. S., Karthick, K., Arunbharathi, R., Thangavel, C., Ananth, S., Prakash, N. N. and Mayakannan, S., Enhancing Mechanical Properties of Polyethylene-Based Nanocomposites using Graphene Nanosheets, Jute Fiber and Polyethylene-Grafted Maleic Anhydride: An RSM Approach, *Int. J. Veh. Struct. Syst.*, 17(5), 920–928 (2025). https://doi.org/10.4273/ijvss.17.5.30

Rajakumar, M. P., Senthil Kumar, S., Srimanickam, B., Srividhya, S., Elangovan, K., Kaliappan, N. and Kamakshi, P. K., Performance enhancement of photovoltaic thermal collectors using water based MnO_2 nanofluids and machine learning models, *Sci. Rep.*, 15(1), 39826 (2025). https://doi.org/10.1038/s41598-025-23505-x

Ramalho, L. B., Portela, J. C., Gondim, J. E. F., da Silva, T. E. M., Filho, M. F. C., de Sousa, L. V, da Silva Ribeiro, J. E., da Silva, E. F., da Silva Dias, N., de Assis de Oliveira, F., da Silva, A. C., de Lima Dias, V., de Oliveira Gomes, D. V, de Morais, M. C., de Luna, S. A. G. and de Sousa, A. L. F., Interactions between soil functional components and micromorphology in different land uses in a mountainous region of northeastern Brazil, *Sci. Tot.*

Environ., 1027, 181724 (2026). https://doi.org/10.1016/j.scitotenv.2026.181724

Rangseesuriyachai, T., Loythala, K., Pinpatthanapong, K., Jongsomjit, B. and Juntadech, N. C., Dynamic adsorption behavior of Pb (II) onto Napier grass-derived carboxymethyl cellulose, *Mater. Chem. Phys.*, 362, 132701 (2026). https://doi.org/10.1016/j.matchemphys.2026.132701

Shen, M. S., Shen, M. Y., Wu, H. C. and Chu, C. Y., Sustainable agent of compost-derived bacteria for enhanced biological hydrolysis and saccharification of Napier grass, *Biores. Technol.*, 442, 133698 (2026). https://doi.org/10.1016/j.biortech.2025.133698

Sonya, A., Kalarani, P., Maheskumar, P., Selvam, P. M. S., Sathish, M., Vimalanathan, P. and Mayakannan, S., Optimization of Tensile Strength in Nano Silica and Calotropis Gigantea Reinforced Hybrid Polymer Nanocomposites using ANN-BBD Modelling, *Int. J. Veh. Struct. Syst.*, 17(4), 680–688 (2025). https://doi.org/10.4273/ijvss.17.4.22

Sucinda, E. F., Abdul Majid, M. S., Ridzuan, M. J. M., Cheng, E. M., Alshahrani, H. A. and Mamat, N., Development and characterisation of packaging film from Napier cellulose nanowhisker reinforced polylactic acid (PLA) bionanocomposites, *Int. J. Biol. Macromol.*, 187, 43–53 (2021). https://doi.org/10.1016/j.ijbiomac.2021.07.069

Sureshkumar, V., Lingeshwaran, P., Vasanthakumar, R., Pradeep, M. K., Prabhu, T., Girimurugan, R. and Kelin, J. S., Development and performance evaluation of hybrid natural fiber sandwich composites for sustainable roofing applications using ann-based prediction, *Interact.*, 247(1), 142 (2026). https://doi.org/10.1007/s10751-026-02498-7

Thaisungnoen, K., Umar, M., Singh, M. and Anal, A. K., Ultrasonic-Assisted Extraction of Bioactive Extract from Napier Grass (Pennisetum purpureum), Evaluation of Its Bioactivity, Antimutagenicity and Cytotoxicity, *Nat. Life Sci. Commun.*, 23(1), (2024). https://doi.org/10.12982/NLSC.2024.014

Thandavamoorthy, R. and Devarajan, Y., Study on the characteristics of Napier grass fibre reinforced porcelain filler particulates poly lactic acid matrix biocomposite, *J. Reinforced Plast. Compos.*, 44(21–22), 2161–2169 (2025). https://doi.org/10.1177/07316844241253912

Tunali, A. S., Kara, I., Yilmaz, A. and Akar, T., A New Surface Decorated Geopolymer Matrix: Insights and Modeling into Comprehensive Sorptive Decolorization Applications, *ACS Omega*, 11(22), 32636–32651 (2026). https://doi.org/10.1021/acsomega.6c01379

Warade, H., Agrawal, D., Motghare, K. L. and Sakharwade, S. G., Modelling and Optimisation of Anaerobic Digestion Oof Napier Grass in a Continuous Stirred Tank Reactor, *African J. Appl. Res.*, 11(6), 16–35 (2025). https://doi.org/10.26437/wxcsjq74

Warade, H., Ansari, K., Bhaskar, K., Naaz, Z., Khan, M. A., Khan, N. A., Zahmatkesh, S. and Hajiaghaei-Keshteli, M., Optimizing the grass bio methanation in lab scale reactor utilizing response surface methodology, *Biofuels*, 14(7), 721–732 (2023). https://doi.org/10.1080/17597269.2023.2170034

Zhao, J., Cheng, Z., Xu, C. and Long, C., Risk Assessment and Management of Potential Invasive Alien Species: A Study on Cenchrus purpureus in the Gaoligong Mountains, *Land*, 14(11), 2211 (2025). https://doi.org/10.3390/land14112211